Multihazard Scenarios for Regional Seismic Risk Assessment of Spatially Distributed Infrastructure

Nafiseh Soleimani[1]; Rachel A. Davidson, M.ASCE[2]; Craig Davis, M.ASCE[3]; Thomas D. O'Rourke, Dist.M.ASCE[4]; and Linda K. Nozick[5]

Abstract: This paper introduces the multihazard optimization-based probabilistic scenario (multihazard OPS) method to create an ensemble of multihazard scenarios that can be used for efficient evaluation of spatially distributed infrastructure. Each *multihazard scenario* is a map depicting a possible realization of the co-occurring multiple hazard effects associated with a single earthquake, including ground motion intensity contours, liquefaction potential contours, and locations of surface fault rupture. Together, when the small set of multihazard scenarios are combined with their computed weights, they represent the probabilistic hazard in a way that captures spatial correlation, includes multiple hazards, and is computationally efficient. In demonstrating the method for Los Angeles, California, we find a set of 350 multihazard scenarios matches the regional hazard and damage with errors small enough for most practical purposes. Further reduction is possible depending on the desired tradeoff between acceptable errors and computational efficiency. A sensitivity analysis suggests it is important to consider each hazard type in determining the multihazard scenarios, although the outcome is not sensitive to the precision of the weights. **DOI: 10.1061/(ASCE)IS.1943-555X.0000598.**

Introduction

Recognizing their importance in community resilience, spatially distributed infrastructure, such as water supply and electric power networks, has received increasing attention within the earthquake engineering community. Seismic risk assessments of these infrastructures ideally: (1) capture spatial correlation, (2) are probabilistic, (3) are computationally efficient, and (4) address the multiple hazards that co-occur in an earthquake. Unlike risk assessment of a single-location facility, the analysis must address the spatial correlation of the components that comprise an infrastructure system, and thus scenario-based approaches, in which the joint performance of all facilities is assessed for one earthquake at a time, are preferred (Crowley and Bommer 2006; Han and Davidson 2012). As with single-location facilities, probabilistic risk assessment is required to support resource allocation and other decisions because the best designs or policies often differ depending on which earthquake occurs. Although probabilistic seismic hazard analysis methods have been available for years, combining it with scenario-based analysis leads to computational challenges. The most straightforward way to accomplish probabilistic scenario-based analysis is using conventional Monte Carlo simulation, in which a rupture, ground motion, facility damage, and system performance are simulated in turn; the process is repeated many times, and the results are combined. To capture the more intense, less frequent events, however, requires many replicates. With computationally intensive models of system performance (e.g., traffic model for the highway system), this approach becomes highly inefficient if not intractable. Finally, in many regions and for some infrastructure types, liquefaction, surface fault rupture, and landslide can cause substantial damage in addition to ground motion. For buried pipelines and roads, in particular, these collateral hazards have represented a major portion of the damage (e.g., O'Rourke et al. 2014). For a complete risk assessment, all relevant hazards should be included.

Recent work has addressed the first three issues—spatial correlation, probabilistic analysis, and computational efficiency—by developing methods to identify a computationally efficient set of earthquake rupture or ground motion scenarios, each with a hazard-consistent annual occurrence probability, that can be used for probabilistic analysis of spatially distributed infrastructure ("Computationally Efficient Probabilistic Approaches for Spatially Distributed Infrastructure" section). The methods perform well, but almost always address only ground motion. In parallel, research has expanded typical ground motion analyses to include collateral hazards like landslide and liquefaction ("Risk Assessment with Multiple Hazards" section), but those studies have not been fully probabilistic. This paper contributes to the literature by integrating these two lines of research to develop a method for multihazard probabilistic seismic hazard analysis for spatially distributed infrastructure. It builds on the extended optimization-based probabilistic scenario (OPS) method from Han and Davidson (2012) and Manzour et al. (2016), but expands it to make it multihazard, specifically to include ground motion, liquefaction, and surface fault rupture hazards in an integrated way. The method is applied to the City of Los Angeles, California. In the case study, we demonstrate the method, examine if including multiple hazards requires more scenarios to match the probabilistic hazard than when ground motion alone is addressed, and assess the extent to which developing an ensemble of multihazard scenarios by matching one hazard type indirectly achieves a good match for others.

[1]Graduate Student, Dept. of Civil and Environmental Engineering, Univ. of Delaware, Newark, DE 19711. Email: nafisehs@udel.edu

[2]Professor, Dept. of Civil and Environmental Engineering, Univ. of Delaware, Newark, DE 19711 (corresponding author). ORCID: https://orcid.org/0000-0002-6061-5985. Email: rdavidso@udel.edu

[3]Engineer, C. A. Davis Engineering, 27017 Vista Encantada Dr., Santa Clarita, CA 91354. Email: cadavisengr@yahoo.com

[4]Professor, School of Civil and Environmental Engineering, Cornell Univ., Ithaca, NY 14853. Email: tdo1@cornell.edu

[5]Professor, School of Civil and Environmental Engineering, Cornell Univ., Ithaca, NY 14853. Email: lkn3@cornell.edu

Note. This manuscript was submitted on April 7, 2020; approved on October 12, 2020; published online on January 13, 2021. Discussion period open until June 13, 2021; separate discussions must be submitted for individual papers. This paper is part of the ***Journal of Infrastructure Systems***, © ASCE, ISSN 1076-0342.

Key strengths of the new multihazard OPS method include the following. First, it generates a relatively small, user-specified number of multihazard scenarios, each with an associated hazard-consistent annual occurrence probability, and each of which represents a physically realistic description of ground motion, liquefaction, and surface fault rupture that could co-occur in a single event. Together, the set of multihazard scenarios (on the order of a few hundred for a large, seismically-active city) are determined so as to minimize the error between (1) the probabilistic ground motion, liquefaction, and surface fault rupture hazard based on the reduced set and (2) that based on a full conventional Monte Carlo simulation. Second, the tradeoff between the error and the number of multihazard scenarios included in the reduced set is explicit, allowing the user to decide the appropriate balance for a given application. Third, once the reduced set of multihazard scenarios is determined for a city or region, it can be used for seismic risk analyses for all aspects of the city (e.g., utility and transportation networks, buildings) to ensure consistency and minimize repetition of effort. Following a summary of the relevant literature, the new multihazard OPS method is presented. This is followed by a description of a case study for Los Angeles, and the paper concludes with suggested avenues of future research.

Literature Review

Computationally Efficient Probabilistic Approaches for Spatially Distributed Infrastructure

Recognizing the computational demands of conventional Monte Carlo simulation (MCS), Chang et al. (2000) introduced the idea of selecting a relatively small set of earthquake scenarios (defined by a source-magnitude combination) and assigning each a hazard-consistent annual occurrence probability. That set is then used for a risk analysis instead of the full set of simulated scenarios. Each hazard-consistent annual occurrence probability can be thought of as a weight. It is not the actual likelihood of occurrence of the associated earthquake, but rather an artificial probability assigned so that the probabilistic combination of the selected set of earthquake scenarios matches hazard maps based on a full probabilistic seismic hazard analysis using a typical discretization approach (which we call PSHA) or conventional MCS.

Jayaram and Baker (2010) extended the idea to include selection of a reduced set of ground motion scenarios with associated hazard-consistent occurrence probabilities. They also advanced it by introducing importance sampling to efficiently generate the candidate sets of earthquake scenarios and ground motion maps, and using a k-means clustering approach to simultaneously select the reduced set of ground motion maps and assign the hazard-consistent annual occurrence probabilities. The extended OPS method further advanced the idea, providing a reproducible method based on a mixed integer linear program that guarantees the minimum error between the reduced set of ground motion scenarios and a full PSHA, and that explicitly characterizes the magnitude and nature of those errors (Vaziri et al. 2012; Han and Davidson 2012; Manzour et al. 2016). Zolfaghari and Peyghaleh (2016) offered a similar application for Tehran, Iran, and Apivatanagul et al. (2011) applies a similar method to hurricane wind and coastal flooding. Christou et al. (2018) describes Hazard Quantization, a method similar to k-means clustering but derived from the concept of continuous random fields. Finally, Miller and Baker (2015) extend these ideas to probabilistic damage scenarios that can further improve efficiency in a risk analysis for spatially distributed infrastructure, using exceedance rates instead of exceedance probabilities.

These methods accomplish the goal of computationally tractable, scenario-based, probabilistic seismic hazard analysis. Using the extended OPS method in an application in the highly seismic area of Christchurch, New Zealand, just 125 ground motion scenarios matched the hazard curves and loss exceedance curves based on a million-year simulation with errors insignificant for practical purposes (Manzour et al. 2016). With the exception of Du and Wang (2014), which applies the extended OPS method with the addition of slope displacement, all of these studies address only the transient ground movement hazard. In this paper, we build on the extended OPS method.

Risk Assessment with Multiple Hazards

Other research is developing methods to address multiple hazards. These multihazard approaches include two distinct situations—combining diverse hazards (e.g., earthquake, wildfire, hurricane) because they can occur in the same region (e.g., Greiving 2006; Salman and Li 2018), and integrating hazards because one triggers another or they co-occur (e.g., earthquake ground motion triggering landslide or liquefaction) (Kappes et al. 2012). For the latter, the multiple hazards can be part of a single complex event.

Recent efforts to address multiple hazards in the context of spatially distributed infrastructure systems include analyses of ground motion, flood, and landslide hazards for transportation networks in Europe (Clarke and Obrien 2016; INFRARISK 2019); ground motion, liquefaction, post-earthquake fire hazards for gas pipelines in Tehran (Omidvar and Kivi 2016); ground motion and hurricane wind hazards for electric power transmission systems (Salman and Li 2018); and earthquake ground motion, liquefaction, and landslide hazards for gas pipelines (De Risi et al. 2018). With a focus on integrating the models of different hazards, however, these studies have not typically emphasized an effort to simultaneously make the analysis efficiently probabilistic. Instead, De Risi et al. (2018) and Omidvar and Kivi (2016), for example, limit their analyses to a single earthquake scenario or fault, including uncertainty in ground motion and component damage, but not rupture. As the former notes, they are appropriate for post-event analysis, but for a long-term risk analysis that considers all possible ruptures, they would be too computationally intensive. Even with importance sampling, a seismic analysis for Christchurch, New Zealand resulted in approximately 75,000 rupture scenarios (Manzour et al. 2016). At the almost 20 min per run for one rupture that De Risi et al. (2018) reports, it would be infeasible to apply for all of them.

Multihazard OPS Method

The multihazard OPS method is similar to that in Manzour et al. (2016), but modified to address multiple, co-occurring earthquake-related hazards. Whereas Manzour et al. (2016) and other methods aimed to produce a set of earthquake scenarios (defined by source and magnitude) and/or ground motion scenarios, the multihazard OPS method output is a small set of multihazard scenarios, each with an associated hazard-consistent annual occurrence probability. A multihazard scenario n is a map depicting a possible realization of the multiple hazard effects associated with a single earthquake, including ground motion intensity, liquefaction potential, and surface fault rupture (Fig. 1). The hazard-consistent annual occurrence probability P_n can be thought of as a weight. Together, when the small set of multihazard scenarios are combined with their weights, they represent the probabilistic hazard in a way that captures spatial correlation, includes multiple hazards, and is computationally efficient.

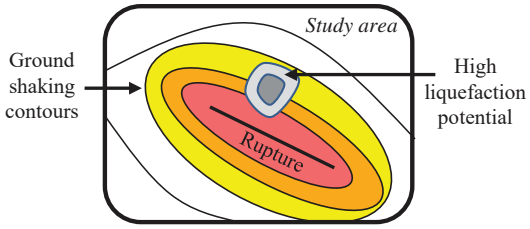

Fig. 1. (Color) Schematic figure of a multihazard scenario.

Specifically, for ground motion, the reduced set of multihazard scenarios match as well as possible the true hazard curves (i.e., those based on a conventional PSHA or MCS) and the true spatial correlation (i.e., that based on a conventional MCS). The matches are defined at a set of specified sites i, and a set of specified points on the hazard curves (defined by the corresponding return periods r). Similarly, for liquefaction, the reduced set of multihazard scenarios match as well as possible the true liquefaction hazard curves and spatial correlation, although the specified sites and return periods may or may not be the same as those for ground motion. For surface fault rupture, the reduced set of multihazard scenarios match as well as possible the true probability of rupture on specified critical faults. The method also provides errors in the hazard curve, spatial correlation, and rupture probability matches.

We consider ground motion, liquefaction, and surface fault rupture hazards, three of the most consequential hazards. The method could be extended further, however, to consider additional collateral hazards, such as landslide or tsunami inundation. We expect that as more hazards are included, more multihazard scenarios will be required to achieve the same match.

Component Hazard Models

Including multiple hazards requires a component hazard model for each. Any metric can be used for ground motion intensity (e.g., peak ground acceleration, spectral acceleration) as long as there is a model to compute it. Ground motion prediction equations (GMPEs) will typically be used, although the method could be adapted to apply physics-based models.

A second model is required to compute liquefaction potential and/or intensity at each site in the region for a specified earthquake and ground motion scenario. Liquefaction susceptibility describes characteristics of the soil that make it more or less prone to liquefaction. When subjected to sufficiently strong ground motion, liquefaction can be triggered in susceptible soil, subsequently potentially producing permanent ground deformation (PGD). Liquefaction potential depends on the combination of liquefaction susceptibility and ground motion. Metrics that could be used to describe liquefaction potential or intensity include probability that liquefaction occurs (e.g., Zhu et al. 2017; Kayen et al. 2013; FEMA 2003), liquefaction potential index (LPI) (Iwasaki et al. 1984; Maurer et al. 2014); factor of safety for liquefaction (e.g., Mayfield et al. 2010); a binary indicator variable (liquefaction/no liquefaction); and PGD caused by liquefaction (e.g., Baska 2003; Youd et al. 2002). The liquefaction model employed should: (1) be able to predict liquefaction potential/intensity at each site in the study region as accurately as possible, (2) describe liquefaction in terms of the desired metric, and (3) be applicable throughout the whole study region, which means that all required input data are available throughout the region. If the intent is to use the multihazard scenarios to estimate damage to pipelines or buildings, the liquefaction measure used must be the same as (or able to be translated into) that used in the damage model. Because most methods require site-specific geotechnical data such as cone penetration test (CPT) or standard penetration test (SPT) results, which are not typically available for an entire region, this final requirement can be limiting.

Although it is often omitted in favor of focus on more geographically widespread effects like ground motion, the surface fault rupture hazard can be important, especially for long ruptures that could simultaneously damage pipelines or other infrastructure in multiple places in a single event. Surface fault rupture hazard differs from ground motion and liquefaction because it is localized along the length of a fault rupture, and therefore must be modeled differently. Multiple earthquakes can cause ground motion and/or liquefaction at a site, allowing the method to match the probabilistic hazard by determining hazard-consistent probabilities in a way that eliminates some earthquakes and weighs others heavily. By contrast, at a particular site, typically only one earthquake-generating source could cause the permanent ground deformation associated with fault rupture. Thus, the only way to match the probability of surface rupture displacement at a site is to include a rupture on that fault in the final reduced set of multihazard scenarios. It is impossible, therefore, to match the surface fault rupture hazard everywhere in the study area with a small set of scenarios. Instead, we focus on a small user-identified set of faults that are of particular concern and we require the reduced set of multihazard scenarios to match the probability of rupture on those faults only. Surface fault rupture intensity can be measured as a binary variable (occurs or not) or in terms of the resulting permanent ground displacement (e.g., Petersen et al. 2011). As with liquefaction and ground motion, the best surface fault rupture hazard model depends on predictive power, availability of the required input data, and output metric required for use in subsequent analyses.

Step-by-Step Implementation

The multihazard OPS method includes five main steps, adapted from Manzour et al. (2016) (Fig. 2): (1) generate a candidate set of earthquake scenarios (ruptures), (2) reduce the set of earthquake scenarios based on their contribution to the ground motion and liquefaction hazards, (3) reduce it and assign hazard-consistent annual occurrence probabilities using a mixed integer linear program (MILP), (4) generate multihazard scenarios for each earthquake scenario in the reduced set in a way that minimizes sampling variability, and (5) reduce the multihazard scenarios using the same MILP from Step 3. Han and Davidson (2012) and Manzour et al. (2016) include additional detail; this section highlights aspects that are new.

Step 1: Generate Candidate Set of Earthquake Scenarios

We first generate an initial candidate set of N_{qc} earthquake scenarios. In general, this is done by sampling events for each earthquake fault or area source based on the associated magnitude-frequency distribution, using importance sampling of the magnitudes to more efficiently include higher magnitude events of greatest consequence (Han and Davidson 2012). (Note that, in the case study herein, we use a different earthquake scenario generation approach for fault sources so as to be consistent with the recent 2014 National Seismic Hazard Map.) The user also identifies and includes in the candidate set any particular earthquake scenarios that are of interest due to their potential surface fault rupture hazard. Importantly, there is no single best candidate set of earthquake scenarios, so the method used is not critical (Vaziri et al. 2012). The candidate set should include only physically realistic earthquakes and should be sufficiently large and diverse that the hazard curves can be

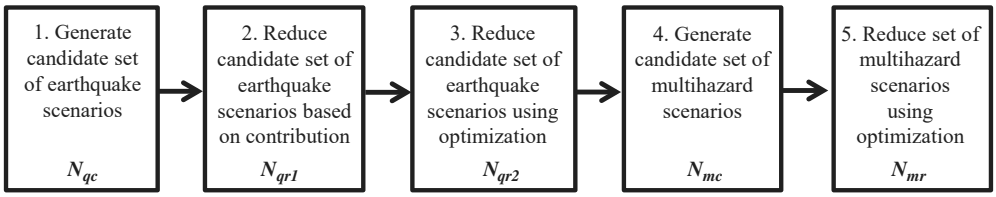

Fig. 2. Main steps in multihazard optimization-based probabilistic scenario (OPS) method.

matched. Beyond that, it does not matter because only a small number will be included in the final reduced set anyway.

Step 2: Reduce Candidate Set of Earthquake Scenarios Based on Contribution

In Step 2, we reduce the candidate set of earthquake scenarios by removing any that are not among those that contribute most to the ground motion or liquefaction hazard. The contributions, $C_{G,j}$ and $C_{L,j}$, of each earthquake scenario j to the ground motion and liquefaction hazard, respectively, are defined as

$$C_{G,j} = \sum_{i=1}^{I_G} \sum_{r=1}^{R_G} \omega_{G,ir} \left[\frac{P_j P(y_{ij} \geq Y_{ir})}{\sum_{j'=1}^{J} P_{j'} P(y_{ij'} \geq Y_{ir})} \right] \quad (1a)$$

$$C_{L,j} = \sum_{i=1}^{I_L} \sum_{r=1}^{R_L} \omega_{L,ir} \left[\frac{P_j P(l_{ij} \geq L_{ir})}{\sum_{j'=1}^{J} P_{j'} P(l_{ij'} \geq L_{ir})} \right] \quad (1b)$$

where P_j = annual occurrence probability of earthquake scenario j; Y_{ir} = true ground motion for return period r at site i; y_{ij} = ground motion at site i caused by earthquake scenario j; L_{ir} = true liquefaction potential for return period r at site i; l_{ij} = liquefaction potential at site i caused by earthquake scenario j; J = number of earthquake scenarios (same as N_{qc}); $0 \leq \omega_{G,ir} \leq 1$ and $0 \leq \omega_{L,ir} \leq 1$ = user-specified weights that can be used to give extra weight to certain sites and/or return periods if desired, such that $\sum_{ir} \omega_{G,ir} = 1$ and $\sum_{ir} \omega_{L,ir} = 1$; I_G and I_L = number of sites for the ground motion and liquefaction hazard, respectively; and R_G and R_L = number of return periods for the ground motion and liquefaction hazard, respectively. The $P(y_{ij} \geq Y_{ir})$ are computed by integrating over the ground motion prediction equations. [Note that although the $P(y_{ij} \geq Y_{ir})$ values are conditional probabilities more completely written as $P(y_{ij} \geq Y_{ir} | Scenario\ j)$, for brevity and to remain consistent with Han and Davidson (2012) and Manzour et al. (2016), we use the notation $P(y_{ij} \geq Y_{ir})$]. Uncertainty in l_{ij} depends only on earthquake magnitude and ground motion intensity [so to compute $P(l_{ij} \geq L_{ir})$, for each possible magnitude, we calculate the ground motion intensity $Y_{L_{ir}}$ associated with L_{ir} and then find $P(y_{ij} \geq Y_{L_{ir}})$].

To ensure earthquake scenarios are retained if they contribute greatly to either the ground motion or liquefaction hazard, all candidate earthquake scenarios are ranked from largest to smallest based on $\max(C_{G,j}, C_{L,j})$. Only those that together account for the top $T\%$ of total ground motion contribution and the top $T\%$ of liquefaction contribution are retained. At the end of Step 2, N_{qr1} earthquake scenarios remain. Note that different thresholds T could be used (Manzour et al. 2016). Conceptually, Step 2 is not required because Step 3 will reduce the candidate set of earthquake scenarios again anyway. It is recommended, however, because it makes the optimization in Step 3 easier to solve computationally, the scenarios omitted in Step 2 contribute so little to the hazard curves that their removal has little effect, and it adds little time since the required probabilities, $P(y_{ij} \geq Y_{ir})$. and $P(l_{ij} \geq L_{ir})$, have to be computed for Step 3 anyway.

Step 3: Reduce Candidate Set of Earthquake Scenarios using Optimization

In Step 3, a mixed-integer linear program is used to further reduce the candidate set of N_{qr1} earthquake scenarios to smaller user-specified N_{qr2} and to assign a hazard-consistent annual occurrence probability, P_j, to each remaining earthquake scenario [Eqs. (2)–(13)]. The optimization is like that in Han and Davidson (2012) and Manzour et al. (2016) except that new constraints are added to define errors in liquefaction and surface fault rupture hazard, and those errors are added to the objective function so that the optimization aims to reduce them as well as errors in the ground motion hazard curves.

Minimize

$$k_G \sum_{i \in I_G} \sum_{r \in R_G} w_{G,ir} (e^+_{G,ir} + e^-_{G,ir}) + k_L \sum_{i \in I_L} \sum_{r \in R_L} w_{L,ir} (e^+_{L,ir} + e^-_{L,ir}) + k_s \sum_{f \in F} w_{S,f} (e^+_{s,f} + e^-_{s,f}) \quad (2)$$

such that

$$\sum_{j=1}^{J} \{P_j \times P(y_{ij} \geq Y_{ir})\} - e^+_{G,ir} + e^-_{G,ir} = 1 - e^{-1/r} \quad \forall\ i \in I_G, r \in R_G \quad (3)$$

$$\sum_{j=1}^{J} \{P_j \times P(l_{ij} \geq L_{ir})\} - e^+_{L,ir} + e^-_{L,ir} = 1 - e^{-1/r} \quad \forall\ i \in I_L, r \in R_L \quad (4)$$

$$\sum_{j \in J_f} P_j - e^+_{s,f} + e^-_{s,f} = P_{t,f} \quad \forall\ f \in F \quad (5)$$

$$\sum_{j \in J_f} z_j \geq 1 \quad \forall\ f \in F \quad (6)$$

$$P_j \leq z_j \quad \forall\ j \quad (7)$$

$$\sum_{j=1}^{J} z_j \leq J_r \quad (8)$$

$$e^+_{G,ir}, e^-_{G,ir} \geq 0 \quad \forall\ i \in I_G, r \in R_G \quad (9)$$

$$e^+_{L,ir}, e^-_{L,ir} \geq 0 \quad \forall\ i \in I_L, r \in R_L \quad (10)$$

$$e^+_{s,f}, e^-_{s,f} \geq 0 \quad \forall\ f \in F \quad (11)$$

$$0 \leq P_j \leq 1, z_j \in \{0, 1\} \quad \forall\ j \quad (12)$$

The objective [Eq. (2)] is to minimize the weighted errors in the ground motion, liquefaction, and surface fault rupture hazards. The user-specified constants, k_G, k_L, and k_S, allow the user to stipulate the relative importance of matching the three types of hazard.

As in Manzour et al. (2016) and Han and Davidson (2012), the ground motion error term is the weighted sum of errors over all sites i and return periods r, between points on the true ground motion hazard curves and the corresponding points on hazard curves developed with the reduced set of earthquake scenarios and the hazard-consistent annual occurrence probabilities. The first term in Eq. (3) is the annual probability of exceeding Y_{ir} as estimated based on the reduced set of multihazard scenarios. Thus, $e^{+}_{G,ir}$ and $e^{-}_{G,ir}$ are the errors resulting from overestimating and underestimating, respectively, the true annual exceedance probability, $1-\exp(-1/r)$, for return period r at site i. The errors $e^{+}_{G,ir}$ are positive if the true values are overestimated and zero otherwise; $e^{-}_{G,ir}$ are positive if the true values are underestimated and zero otherwise. The liquefaction error term is analogous to the ground motion error term. The liquefaction potential errors, $e^{+}_{L,ir}$ and $e^{-}_{L,ir}$, are similarly the over and underestimation of liquefaction potential for return period r at site i [Eq. (4)]. Note that the sites and return periods used to match ground motion and liquefaction need not be the same. Because liquefaction will likely be physically impossible at some locations and vary more locally than ground motion in others, the set of sites considered in matching liquefaction potential, I_L, will likely be smaller than that for ground motion, I_G. The user-specified weights $w_{G,ir}, w_{L,ir} \geq 0$ are typically set to $w_{G,ir} = w_{L,ir} = r$ to give equal weight to each error as a percentage of its true exceedance probability (Manzour et al. 2016). If desired, they could be set to vary by site to indicate locations that are more or less important to match (as in Legg et al. 2010).

The surface fault rupture error is defined differently than ground motion and liquefaction errors because at a particular site, typically only one earthquake generating source could cause the permanent ground deformation associated with fault rupture. Thus, we define the surface fault rupture error in terms of the difference, for each fault in F, between the true annual occurrence probability, $P_{t,f}$, and the hazard-consistent annual occurrence probability based on the reduced set, $\sum_{j\in J_f} P_j$ [Eq. (5)], where F is the user-specified set of faults considered important for surface fault rupture hazard and J_f is the set of all earthquake scenarios j with at least one segment on fault f. The user-specified weight $w_{S,f} \geq 0$ should typically be set to $w_{S,f} = 1/P_{t,f}$ to normalize the surface fault rupture errors so they are approximately the same order of magnitude as the ground motion and liquefaction errors and the k weights can represent relative importance of the different hazards. With z_j defined as a binary variable that indicates whether earthquake scenario j is included in the reduced set of events, Eq. (6) (which is optional depending on user preferences) ensures that at least one earthquake is included for each fault in J_f; and Eqs. (7) and (8) limit the number of earthquake scenarios j included in the final reduced set to a user-specified number $J_r = N_{qr2}$.

The optimization provides as output values for the decision variables P_j, which define the new hazard-consistent annual occurrence probability for earthquake scenario j. If $P_j = 0$, scenario j is not included in the reduced set. It also provides values of all the errors—$e^{+}_{G,ir}$, $e^{-}_{G,ir}$, $e^{+}_{L,ir}$, $e^{-}_{L,ir}$, $e^{+}_{s,f}$, and $e^{-}_{s,f}$, which can be used to ensure that they are of an appropriate size and character for the intended purpose.

Step 4: Generate Candidate set of Multihazard Scenarios

In Step 4, we generate a user-specified N_{mc} candidate multihazard scenarios. Each multihazard scenario is a map that includes (Fig. 1): (1) the surface rupture from the associated earthquake scenario, (2) ground motion contours, and (3) liquefaction potential contours. The ground motion contours are computed using the ground motion prediction equations, and sampling values the residuals. The liquefaction potential contours are computed using the information about the earthquake scenario (e.g., magnitude) and the sampled ground motion map, so that all hazards described in the scenario are internally consistent.

Eq. (13) is used to determine N_j, the number of multihazard scenarios associated with each earthquake scenario j. As derived in Han and Davidson (2012), employing Eq. (13) minimizes the variability in the estimated probability of exceeding ground motion Y_{ir}, while ensuring a total of $N_{mc} \cong \sum_j N_j$ candidate multihazard scenarios are sampled. Using this approach, more multihazard scenarios are sampled from those earthquake scenarios j for which the probability of exceeding a specified ground motion varies a lot across ground motion scenarios. Unlike Manzour et al. (2016), which included fewer earthquake scenarios, here we allow N_j to be zero when rounded

$$N_j = N_{mc}\left[\frac{P_j\sqrt{P(y_{ij} \geq Y_{ir}) \times [1-P(y_{ij} \geq Y_{ir})]}}{\sum_{j'} P_{j'}\sqrt{P(y_{ij'} \geq Y_{ir}) \times [1-P(y_{ij'} \geq Y_{ir})]}}\right] \quad (13)$$

Ground motion is used to determine the number of multihazard scenarios associated with each earthquake scenario in this step because the variability across multihazard scenarios for a specified earthquake scenario is associated with ground motion. In any case, as in Step 1, there is not just one best candidate set. The candidate set need only be large enough and represent enough variability that a reduced set of multihazard scenarios can be identified in Step 5 that minimizes the errors to an acceptable degree.

Step 5: Reduce Candidate Set of Multihazard Scenarios using Optimization

The optimization in Step 3 [Eqs. (2)–(12)] is applied again in Step 5 to reduce the candidate set of N_{mc} multihazard scenarios to a user-specified set of N_{mr} multihazard scenarios that together minimize the error between the description of hazards based on the reduced set and the true description of hazards. The only differences in applying the optimization in this step are that: (1) we replace earthquake scenario j with multihazard scenario n; (2) the user-specified number of scenarios in the reduced set, J_r, is now N_{mr}; and (3) the values of $P(y_{in} \geq Y_{ir})$ and $P(l_{in} \geq L_{ir})$ are binary (zero or one) values since there is no uncertainty in the ground motion or liquefaction potential at site i in multihazard scenario n.

Evaluation Metrics

Results are evaluated using four types of metrics. First, we present the average of the errors for each hazard type in terms of probabilities—Average $e^{+/-}_{G,ir}$, Average $e^{+/-}_{L,ir}$, and Average $e^{+/-}_{s,f}$—the quantities directly being minimized. Second, for errors that are easier to interpret, we use the mean ground motion hazard curve error, $MHCE_G$, and mean liquefaction hazard curve error, $MHCE_L$. $MHCE_G$ is the same metric that was known as $MHCE$ in Han and Davidson (2012) and Manzour et al. (2016). It is the mean over all sites i and return periods r of the ground motion hazard curve errors, $HCE_{G,ir}$, defined as the horizontal distance at return period r from the reduced set hazard curve to the true hazard curve for location i [Eqs. (14) and (15)]. $MHCE_L$ is the analogous metric defined for the liquefaction hazard [Eqs. (16) and (17)]

$$(HCE)_{G,ir} = (Y_{ir} - \hat{Y}_{ir})/Y_{ir} \quad (14)$$

$$MHCE_G = \frac{1}{I_G R_G} \sum_{r_G}^{R_G} \sum_{i_G}^{I_G} |(HCE)_{G,ir}| \quad (15)$$

$$(HCE)_{L,ir} = (L_{ir} - \hat{L}_{ir})/L_{ir} \quad (16)$$

$$MHCE_L = \frac{1}{I_L R_L} \sum_{r_L}^{R_L} \sum_{i_L}^{I_L} |(HCE)_{L,ir}| \quad (17)$$

where Y_{ir}, $\hat{Y}_{ir}$, L_{ir}, and $\hat{L}_{ir}$ are the true and reduced set ground motion intensities, and true and reduced set liquefaction potential index values at site i and return period r, respectively.

Third, we define spatial correlation errors for ground motion and liquefaction hazards as in Han and Davidson [2012, Eqs. (15) and (16)]. Eqs. (18) and (19) define the mean spatial correlation error for ground motion, $MSCE_G$, where ρ_{i_1,i_2}^{true} and $\rho_{i_1,i_2}^{reduced}$ are the weighted correlation coefficients of the ground motions at sites i_1 and i_2, for the true and reduced set, respectively, and the weight for each scenario is its annual occurrence probability. An analogous definition holds for the mean spatial correlation error for liquefaction, $MSCE_L$

$$(SCE)_{G,i_1,i_2} = \rho_{i_1,i_2}^{true} - \rho_{i_1,i_2}^{reduced} \quad (18)$$

$$MSCE_G = \frac{1}{I_G^2 - I_G} \sum_{i_1}^{I_G} \sum_{i_2 \neq i_1}^{I_G} |(SCE)_{G,i_1,i_2}| \quad (19)$$

Finally, to examine the practical implications of replacing a full set of scenarios developed using conventional MCS with a reduced set based on the multihazard OPS method, we compare estimates of number of damaged water pipes from each. Any relevant damage or loss model for any type of infrastructure could be used; this was chosen for our case study as an example because it relies on both ground motion and liquefaction potential. Specifically, using D_n, the expected number of damaged pipes in multihazard scenario n and annual probability P_n for each multihazard scenario n, an empirical CDF of damage is created. The mean damage curve error (MDCE) is then defined as the average absolute error as a percentage, over all exceedance probabilities, where D_e and $\hat{D}_e$ are the true and reduced set number of damaged pipes with annual exceedance probability e, and n_e is the number of probabilities evalauted (every 0.0001 from $1/2,500$ to $1/100$ in the case study)

$$MDCE = \frac{1}{n_e} \sum_e |(D_e - \hat{D}_e)/D_e| \quad (20)$$

City of Los Angeles Case Study

Inputs

The aim of this case study is to demonstrate the multihazard method and examine the effect of considering multiple hazards. The City of Los Angeles, a seismically active region with 4.0 million people in an area of $1,300$ km^2, serves as the case study region (US Census Bureau 2019). The city was partitioned into $I_G = 369$ 2-km-by-2-km grid cells. Because liquefaction varies at a higher geographic resolution, those ground motion grid cells in areas with nonzero liquefaction susceptibility were partitioned into $I_L = 367$ 1-km-by-1-km grid cells. The liquefaction susceptible areas were identified based on liquefaction hazard zone 7.5-min quadrangle maps prepared by the California Geologic Survey, which in turn were used to develop the 21 liquefaction susceptibility maps covering Los Angeles over the period 2001–2003 (SCG 2003). The hazard curve values for matching both ground motion and liquefaction were calculated at the same four return periods of $r = 100$, 475, 1,000, and 2,500 years, as in Han and Davidson (2012). In Step 2, the weights $\omega_{G,ir}$ are assumed to all be equal; the same is true for $\omega_{L,ir}$. For the base case, the user-specified relative hazard weights were $k_G = k_L = k_S = 1/3$, corresponding to an assumption of equal importance across all three hazard types. Other values were tested in the sensitivity analysis.

Earthquake Sources

All earthquake source and ground motion inputs were identified so as to be consistent with the most recent 2014 National Seismic Hazard Map (NSHM), which is based on the Uniform California Earthquake Rupture Forecast v3 (UCERF3) (Petersen et al. 2011; Field et al. 2014; Powers 2015). To relax fault segmentation assumptions and include multifault ruptures, UCERF3 makes a substantial departure from previous methods (including those used in Han and Davidson 2012). Rather than constructing a magnitude-frequency distribution model for each fault separately then adding background seismicity, in UCERF3, all fault sections are divided into small equal-length subsections, all plausible combinations of two or more contiguous fault subsections are considered possible ruptures, and the rates of all ruptures are computed simultaneously using the inversion method (Field et al. 2014). UCERF3 results in 250,000+ possible ruptures compared to <8,000 in UCERF2. In this case study, we directly used the 186,716 ruptures from the earthquake rupture forecast that are within 200 km of Los Angeles in the candidate set of earthquake scenarios. In addition, consistent with the 2014 NSHM, background sources are represented as gridded seismicity at 0.1° longitude by 0.1° latitude following truncated Gutenberg–Richter relationships. Including only those within 200 km of Los Angeles resulted in 2,505 background sources.

Component Hazard Models

Ground motion was modeled using the five ground motion prediction equations and weights for the Western US from the 2014 NSHM (table 16 of Petersen et al. 2011). In the case study, we used the ground motion intensity parameter spectral acceleration at 0.2 s, $S_{a,0.2s}$, although another could be substituted.

We compute the liquefaction hazard using the LPI3 model in Kongar et al. (2017). This model was chosen because the data are available to apply it to a large region unlike methods that require CPT, SPT, or other detailed geotechnical data, and because, based on the comparison in Kongar et al. (2017) and our own comparison for the 1994 Northridge earthquake (Soleimani 2020), it offers accuracy that is reasonable for regional analysis like that targeted by the multihazard OPS method. The LPI3 method estimates liquefaction potential in terms of the liquefaction potential index (LPI), which Maurer et al. (2014) interprets as corresponding to no (LPI < 4), marginal ($4 \leq$ LPI < 8), moderate ($8 \leq$ LPI < 15), and severe (LPI $\leq$ 15) liquefaction. The method, which is based on the average shear-wave velocity over the top 30 m of soil, V_{s30}, is a combination of previous work by Seed and Idriss (1971), Andrus and Stokoe (2000), Juang et al. (2005), and Boore (2004). At each location, the soil is partitioned into layers, each $h_k = 5$-m thick, where z_k is the depth to the bottom of layer k and $k = 1$ is the top layer. It requires computing for each layer k: (1) average shear-wave velocities, $V_{s,k}$, and stress-corrected shear-wave velocity, $V_{s1,k}$ [Eqs. (21) and (22)]; (2) cyclic stress ratio, CSR_k [Eqs. (23)–(26)]; and (3) cyclic resistance ratio, CSR_k [Eq. (27)]. We then use Eq. (28) to compute LPI

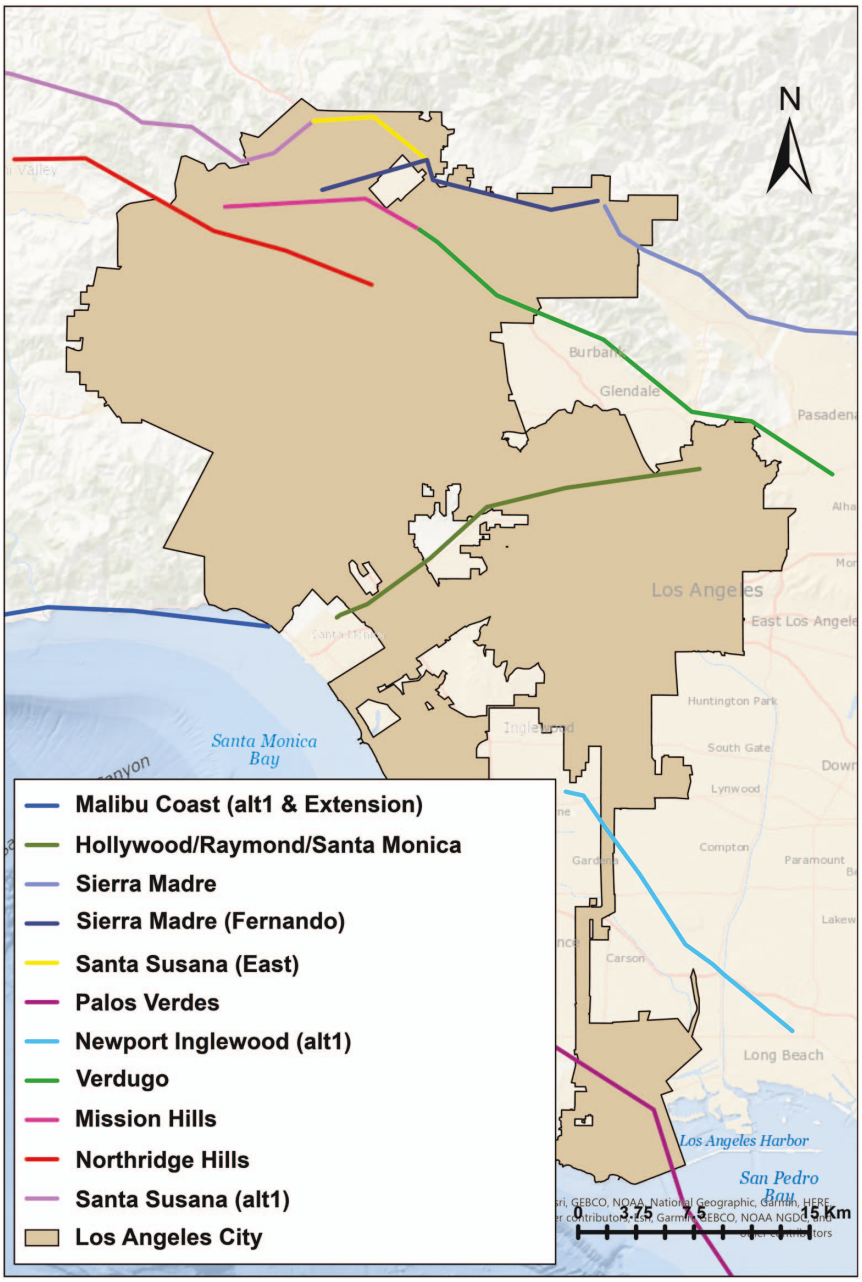

Fig. 3. (Color) Traces of 15 considered faults for surface rupture hazard (Sources: Esri, GEBCO, NOAA, National Geographic, Garmin, HERE, Geonames.org, and other contributors, Esri, Garmin, GEBCO, NOAA NGDC, and other contributors.).

$$V_{s,k} = \begin{cases} 10^{\left(\frac{\log V_{s30} - 0.042062}{1.0292}\right)} & \text{for } z_k \le 10 \\ 2\left[10^{\left(\frac{\log V_{s30} - 0.025439}{1.0095}\right)}\right] - 10^{\left(\frac{\log V_{s30} - 0.042062}{1.0292}\right)} & \text{for } 10 < z_k \le 20 \end{cases} \tag{21}$$

$$V_{s1,k} = V_{s,k}\left(\frac{100}{\sigma'_v}\right)^{0.25} \tag{22}$$

$$r_d = \begin{cases} 1 - 0.00765 z_k & \text{for } z_k < 9.2\,m \\ 1.174 - 0.0267 z_k & \text{for } z_k \ge 9.2\,m \end{cases} \tag{23}$$

$$\sigma_{v,k} = \sum_{m=1}^{k} \rho_m h_m g \tag{24}$$

$$\sigma'_{v,k} = \begin{cases} \sigma_{v,k} & \text{for } z_k \le z_{wt} \\ \sigma_{v,k} - \rho_w (z_k - z_{wt}) g & \text{for } z_k > z_{wt} \end{cases} \tag{25}$$

$$CSR_k = 0.65\left(\frac{a_{\max}}{g}\right)\left(\frac{\sigma_{v,k}}{\sigma'_{v,k}}\right) r_d \tag{26}$$

$$CRR_k = \left(0.022\left(\frac{V_{s1,k}}{100}\right)^2 + 2.8\left(\frac{1}{V^*_{s1,k} - V_{s1,k}} - \frac{1}{V^*_{s1,k}}\right)\right)\left(\frac{M_w}{7.5}\right)^{-2.56} \tag{27}$$

$$LPI = \sum_{k=1}^{4}\left(1 - 1.4\frac{CRR_k}{CSR_k}\right)(10 - 0.5 z_k) \tag{28}$$

where r_d = shear stress reduction coefficient; $\sigma_{v,k}$ = total overburden stress at depth z_k in N/m^3; $\sigma'_{v,k}$ = effective overburden stress at depth z_k in N/m^3; ρ_m = soil density of layer m in kg/m^3; ρ_w = 1,000 kg/m^3 is density of water; z_{wt} = water table depth in m; $a_{\max}$ = peak horizontal ground acceleration (PGA) in m/s^2; g = acceleration of gravity; V^*_{s1} = limiting upper value of V_{s1} for cyclic liquefaction occurrence, assumed to be 200 m/s for all sites; and M_w = earthquake moment magnitude. Following Anbazhagan et al. (2016), we assume soil density is $\rho_{dry} = 0.523V_s^{0.193}$ for layers above the water table and $\rho_{sat} = \rho_{bulk} = 0.412V_s^{0.262}$ for those below. The input data required is thus only V_{s30}, z_{wt}, $a_{\max}$, and M_w. The V_{s30} data was taken from Wills and Clahan (2006); z_{wt} was obtained by spatially interpolating over data from California Department of Water Resources (2019); and $a_{\max}$ and M_w are from the earthquake scenario.

The user-specified set of faults considered important for surface rupture hazard, F, was defined with input from the Los Angeles Department of Water and Power (LADWP) (Davis 2019). It was taken to include the following 15 faults (with number of earthquake scenarios in associated set J_f): Hollywood (771); Malibu Coast [alt1 (460) and extension (364)]; Mission Hills (160), Newport Inglewood alt1 (520); Northridge Hills (1595); Palos Verdes (169); Raymond (639); Santa Monica (783); Santa Susana [east (256) and alt1 (388)]; Sierra Madre (494); Sierra Madre–San Fernando (84); Verdugo (608); and Hollywood-Raymond-Santa Monica combination (730). These faults include earthquakes of magnitudes 5.80–8.05 (Fig. 3).

True Hazard

The true ground motion and liquefaction hazard were based on conventional MCS because unlike PSHA, MCS allows comparison of the spatial correlation error (Han and Davidson 2012). However, the true ground motion and liquefaction hazard were computed in two parts. The 186,716 UCERF3 fault rupture scenarios were included directly ("Earthquake Sources" section), and a conventional MCS over 200,000 years was applied to generate 157,175 background source scenarios to add to the set.

Pipe Damage Model

To compute the method performance in terms of error in damage estimates, we apply the logistic regression model labeled R3 in Bagriacik et al. (2018) to estimate the expected number of damage pipe segments [Eqs. (29 and (30)], where p_{tin} is the probability a pipe segment of type t in grid cell i breaks in multihazard scenario n; $x_{PGV,in}$ and $x_{LRI,in}$ are the peak ground velocity and liquefaction resistance index (LRI) in grid cell i for multihazard scenario n, respectively; and x_{CI}, x_{AC}, x_{DI}, and x_S are binary variables that are one if the pipe is cast iron (CI), asbestos cement (AC), ductile iron (DI), or steel (S) respectively, and zero otherwise

$$Z = -2.39 + 0.014(x_{PGV,in}) - 0.677(x_{LRI,in}) + 0.014(25) - 0.885x_{CI} - 0.522x_{AC} - 1.74x_{DI} - 0.739x_S \quad (29)$$

$$p_{tin} = \frac{\exp(Z)}{1 + \exp(Z)} \quad (30)$$

The LADWP, which operates the water supply system in the study area, has approximately 11,800 km of distribution mains (LADWP 2017). For simplicity, we assume they are evenly distributed across the city; that each pipe segment, defined as the length between intersections with other pipes, is 25 m long; and that the distribution of materials is the same as at the time of the Northridge earthquake in 1994, 72% CI, 9% AC, 8% DI, and 11% S (O'Rourke et al. 2014). For these purposes—examining the effect of using a reduced set of multihazard scenarios instead of a full set from conventional MCS on pipe damage—these simplifications are reasonable. An evaluation of system functionality would require the actual network. To obtain the $x_{LRI,in}$ values, we save the *CRR* values while computing LPI ("Component Hazard Models" subsection of "Inputs" section) and map CRR to LRI as defined in Cubrinovski et al. (2011). The expected number of damaged pipes in multihazard scenario n is $D_n = \sum_{i,t} p_{tin} N_t$, where N_t is the number of pipe segments of type t in each grid cell.

Application of Method

The method is implemented using Python version 3.5 (python.org) to create and call the optimization model in Steps 3 and 5, and Matlab version R2017b (mathworks.com) for everything else. The optimizations were solved using Gurobi version 8.1, a commercial solver (gurobi.com). To help interpret the results of this analysis, we compare to them to those in Han and Davidson (2012) and Manzour et al. (2016), which apply the ground-motion-only version of the Extended OPS method to Los Angeles and Christchurch, New Zealand, respectively. Han and Davidson (2012) also differs in that it

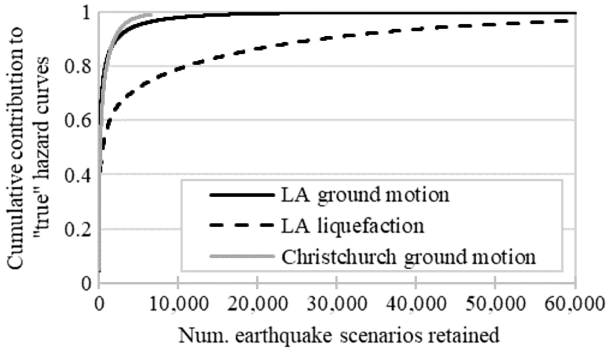

Fig. 4. Cumulative contribution versus number of earthquake scenarios included.

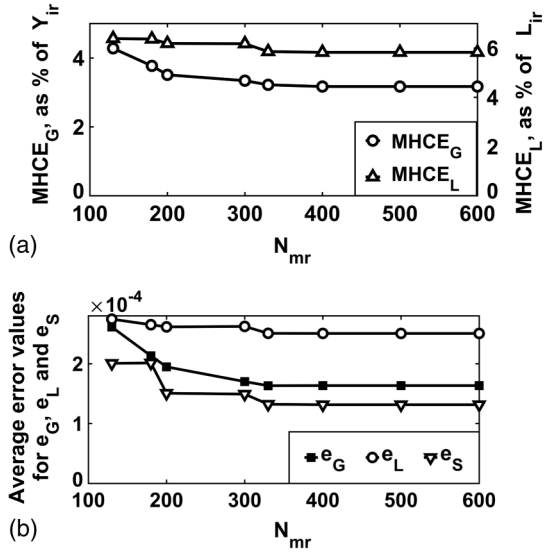

Fig. 5. (a) MHCEG and MHCEL; and (b) average probability errors, both as functions of *Nmr*, the number of multihazard scenarios in the final reduced set.

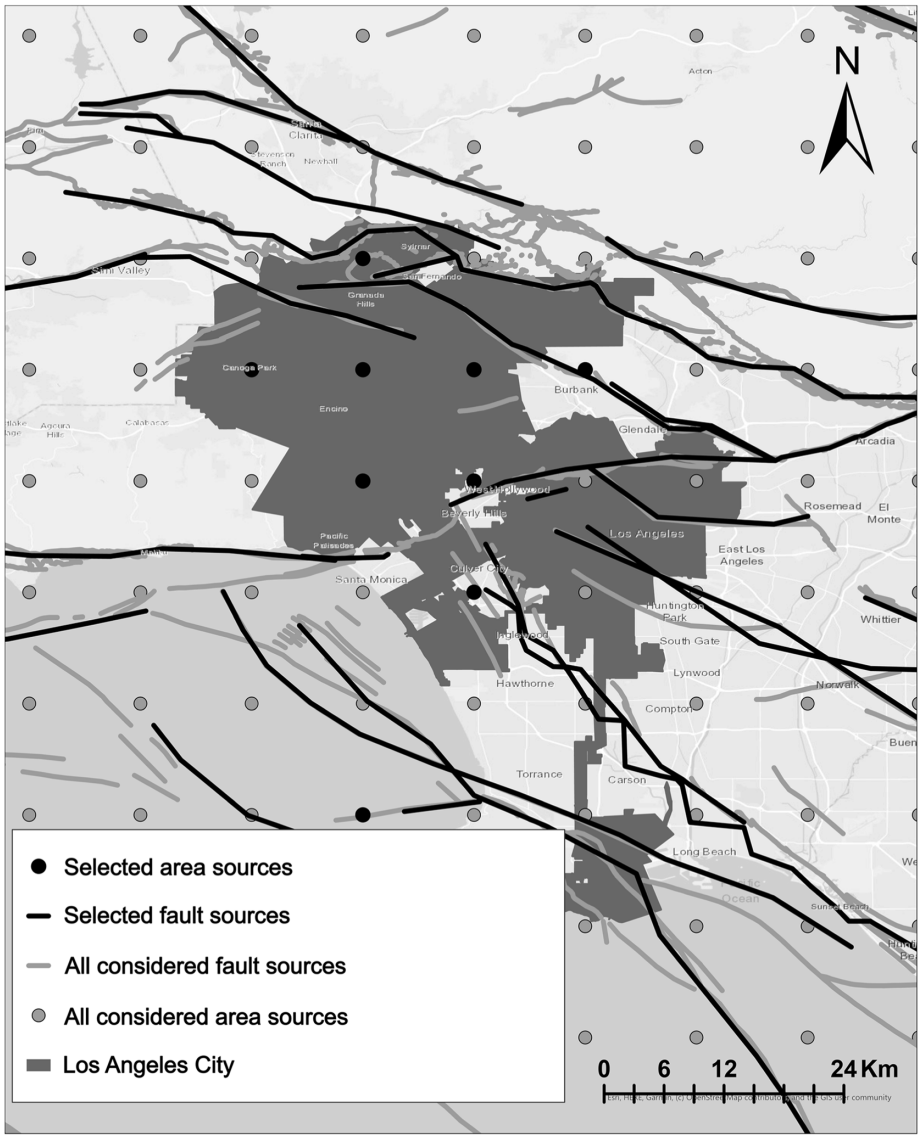

Fig. 6. Map showing the faults and area sources considered and those selected in the final reduced set of 351 multihazard scenarios (Sources: Esri, HERE, Garmin, © OpenStreetMap contributors, and the GIS user community.).

does not include Step 2, and it used input from the 2008 NSHM instead of the substantially modified 2014 NSHM used here.

Step 1: Generate Candidate Set of Earthquake Scenarios

Due to the new way the 2014 NSHM generated earthquake scenarios, we did not have to simulate earthquake scenarios from fault sources. Rather, we directly used the 186,716 ruptures from the 2014 NSHM earthquake rupture forecast that are within 200 km of Los Angeles in the candidate set of earthquake scenarios. Additional candidate earthquake scenarios were generated from the background sources using importance sampling as in Han and Davidson (2012) and Manzour et al. (2016). In doing so, the magnitude range was divided into bins of width 0.1. This approach led to 147,470 background source earthquake scenarios. In total, $N_{qc} = 334{,}186$ candidate earthquake scenarios.

Step 2: Reduce Candidate Set of Earthquake Scenarios Based on Contribution

The first reduced set included $N_{qr1} = 19{,}154$ earthquake scenarios, which was based on ensuring we retained at least $T = 85\%$ of the total contribution for both ground motion and liquefaction hazard.

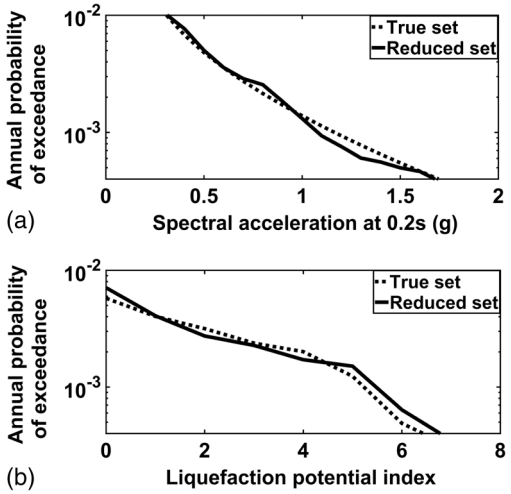

Fig. 7. Comparison of true and reduced set hazard curves, for the sites for which 90% of matches are worse, for (a) ground motion; and (b) liquefaction.

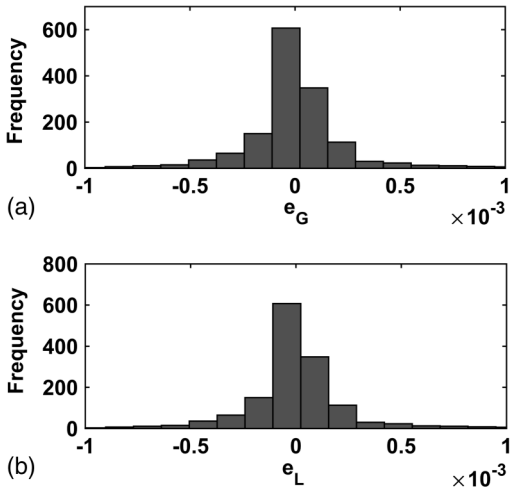

Fig. 8. Histograms of probability errors for (a) ground motion; and (b) liquefaction.

The actual percentages of contribution included for ground motion and liquefaction were 97% and 85%, respectively (Fig. 4). By comparison, in Manzour et al. (2016) 99% of the contribution was retained because that resulted in only 6,500 earthquake scenarios. For both Los Angeles and Christchurch (Manzour et al. 2016) the cumulative contribution curves are much steeper than for liquefaction (Fig. 4). A scatterplot of $C_{L,j}$ versus $C_{G,j}$ suggests that they are highly correlated ($\rho = 0.96$), but the average contribution of each earthquake scenario to the liquefaction hazard is 65% that of the average contribution of each to the ground motion hazard.

Step 3: Reduce Candidate Set of Earthquake Scenarios Based Using Optimization

The maximum number of earthquake scenarios allowed in the second reduced set was taken to be $N_{qr2} = 1,000$, but the optimization selected only $N_{qr2(actual)} = 815$, suggesting that including additional earthquake scenarios would not reduce the error further. The mean errors at this intermediate step were $MHCE_G = 0.025$ and $MHCE_L = 0.061$ meaning that on average, the reduced set ground motion hazard curve based on those 815 earthquake scenarios differed from the true ground motion hazard curve by 2.5%. Similarly, on average, the reduced set liquefaction hazard curve differs by 6.1%. In terms of probabilities, the average absolute value errors were $e_G = 9.3 \times 10^{-7}$, $e_L = 1.6 \times 10^{-6}$, and $e_S = 0$.

By comparison, at this stage in Han and Davidson (2012), the method selected only 143 earthquake scenarios resulting in $MHCE_G = 0.025$ and in Manzour et al. (2016), 83 earthquake scenarios were selected with $MHCE_G = 0.001$. Both those studies considered only ground motion hazard, so they could achieve smaller errors with fewer earthquake scenarios. Nevertheless, these multihazard results were on par with the earlier results at this step, and these intermediate errors appear small enough for practical purposes.

Step 4: Generate Candidate Set of Multihazard Scenarios

We tried five values for the number of candidate multihazard scenarios, N_{mc} (900; 2,000; 3,000; 5,000; 10,000). Ultimately, we set $N_{mc} = 900$ [with the actual number generated $N_{mc(actual)} = 805$], fewer than the $N_{mc} = 2,000$ and $N_{mc} = 3,000$ used in Manzour et al. (2016) and Han and Davidson (2012), respectively. The reasons for the choice were that using $N_{mc} = 900$ resulted in errors small enough for most practical purposes, and the Step 5 optimization did not converge for $N_{mr} \leq 300$ if N_{mc} was higher (e.g., for

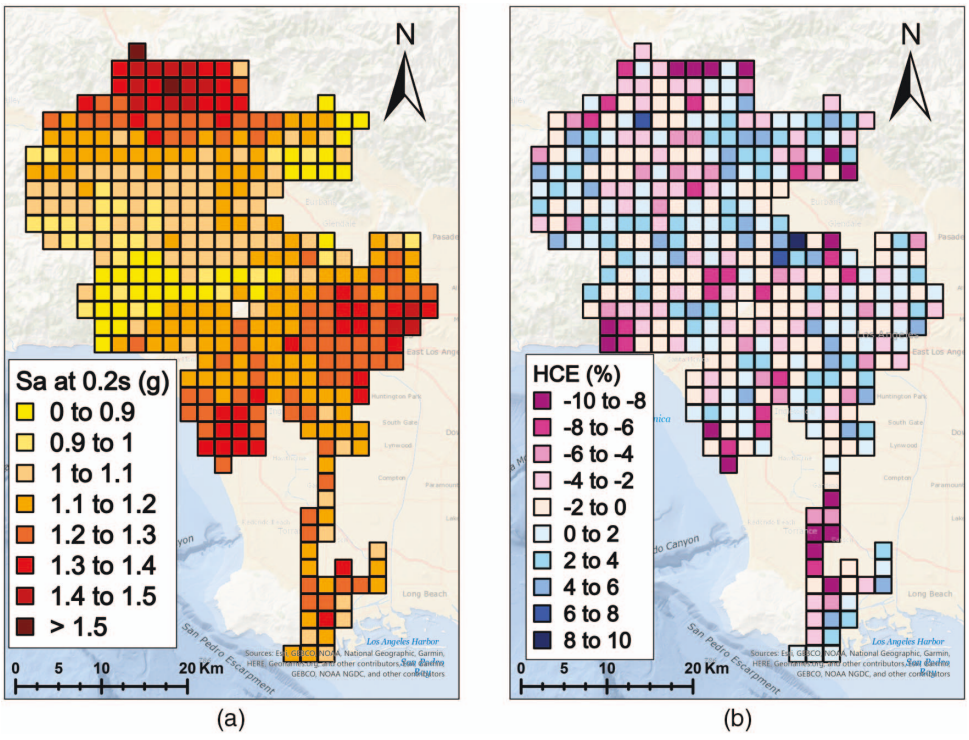

Fig. 9. (Color) Maps of (a) true ground motion Sa (0.2 s); and (b) ground motion hazard curve errors, HCEG, i, 475, for 351 reduced set multihazard scenarios, both for 475-year return period (Sources: Esri, GEBCO, NOAA, National Geographic, Garmin, HERE, Geonames.org, and other contributors, Esri, Garmin, GEBCO, NOAA NGDC, and other contributors.).

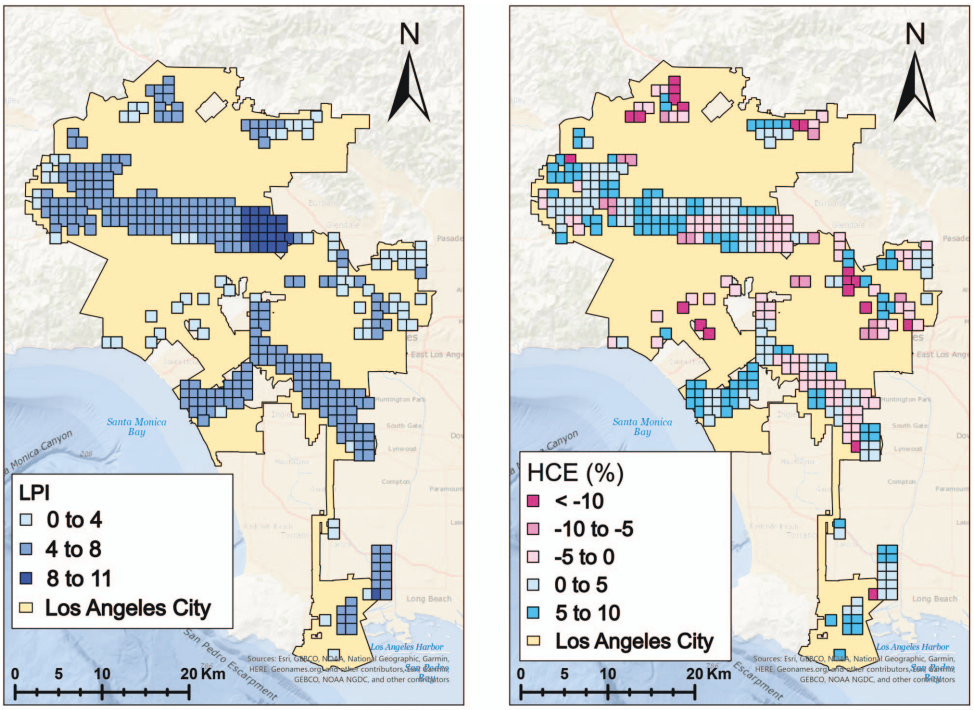

Fig. 10. (Color) Maps of (a) true liquefaction potential, LPI; and (b) liquefaction hazard curve errors, HCEL, i, 475, for 351 reduced set multihazard scenarios, both for 475-year return period (Sources: Esri, GEBCO, NOAA, National Geographic, Garmin, HERE, Geonames.org, and other contributors, Esri, Garmin, GEBCO, NOAA NGDC, and other contributors.).

$N_{mc} = 5{,}000$ and $N_{mr} = 200$ the gap was above 50% after four days). One could explore other solution algorithms to allow for larger N_{mc} values if desired, but that was not necessary for this study.

Step 5: Reduce Candidate Set of Multihazard Scenarios Based Using Optimization

Finally, the maximum number of multihazard scenarios allowed in the final reduced set was varied $N_{mr} = 200$ to 600 to examine the tradeoff between the error introduced and the final number of multihazard scenarios. Fig. 5, which depicts the tradeoffs, suggests that $N_{mr} = 400$, which resulted in $N_{mr(actual)} = 351$, represents a reasonable point in the tradeoff, and thus we use that as the base case.

Results

Final Recommended Set of Probabilistic Multihazard Scenarios

The base case run can be summarized as follows (Fig. 2): $N_{qc} = 334{,}186$ candidate earthquake scenarios; $N_{qr1} = 19{,}154$ earthquake scenarios after reduction based on 85% contribution; $N_{\mathrm{qr2}} = 1{,}000$ earthquake scenarios allowed after reduction using the optimization, $[N_{qr2(\mathrm{actual})} = 815]$; $N_{\mathrm{mc}} = 900$ candidate multihazard scenarios specified $[N_{mc(actual)} = 815]$; and $N_{mr} = 400$ multihazard scenarios allowed in the reduced set $[N_{mr(actual)} = 351]$. The resulting 351 multihazard scenarios range from magnitude of 5.2–7.9, and the adjusted annual occurrence probabilities from 6.065×10^{-7} to 2.464×10^{-3}. They include 338 multihazard scenarios from fault sources and 13 from background sources (Fig. 6).

Performance

To determine how well this reduced set of 351 multihazard scenarios captures the true ground motion, liquefaction, and surface fault ruptures hazards, we examine the evaluation metrics. The probability errors introduced by using the reduced set of 351 multihazard scenarios are: Average $e_G = 1.634 \times 10^{-4}$, average $e_L = 2.506 \times 10^{-4}$, and average $e_S = 1.615 \times 10^{-4}$. These values are small and useful for comparing across runs. Metrics that are easier to interpret are $MHCE_G = 3.2\%$, $MHCE_L = 5.8\%$, which indicate the reduced set ground motion and liquefaction hazard curves differ from the true ones in the horizontal direction by 3.2% and 5.8% on average across all sites i and return periods r. For comparison, Han and Davidson (2012) resulted in 194 ground motion scenarios with $MHCE_G = 0.84\%$, and Manzour et al. (2016) resulted in 124 ground motion scenarios with $MHCE_G = 0$. Spatial correlation errors are $MSCE_G = 0.088$ and $MSCE_L = 0.026$, compared to $MSCE_G = 9.4 \times 10^{-4}$ and $MSCE_G = 0.031$ for Han and Davidson (2012) and Manzour et al. (2016), respectively. To offer

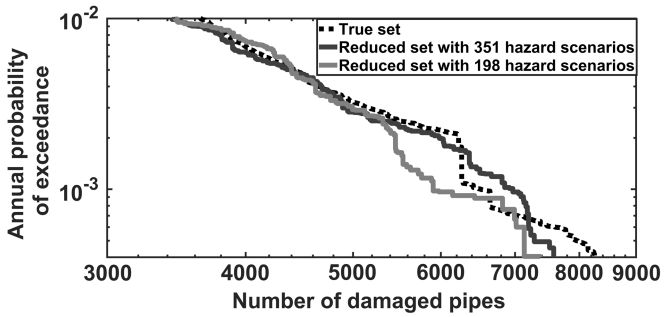

Fig. 11. Comparison of probability distributions of number of damaged pipes based on conventional MCS with 343,891 multihazard scenarios and reduced set of 198 and 351 multihazard scenarios.

Table 1. Results of sensitivity analysis for hazard weights

Run	k_G	k_L	k_S	N_{mr}	$MHCE_G$	$MHCE_L$	Avg.e_G	Avg.e_L	Avg.e_S	MDCE
1	1	0	0	324	0.027	0.271	$1.08(10^{-4})$	0.080	1.07	0.054
2	0	1	0	259	0.571	0.051	1.75	$1.80(10^{-4})$	1.73	0.619
3	0	0	1	15	0.323	0.508	0.246	0.031	0	0.052
4	0.5	0.5	0	306	0.032	0.057	$1.64(10^{-4})$	$2.52(10^{-4})$	1.47	0.046
5	0.5	0	0.5	335	0.029	0.284	$1.11(10^{-4})$	0.075	$0.62(10^{-4})$	0.032
6	0	0.5	0.5	245	0.254	0.048	1.54	$1.92(10^{-4})$	$3.38(10^{-4})$	0.100
7	0.5	0.25	0.25	334	0.032	0.058	$1.47(10^{-4})$	$2.64(10^{-4})$	$2.07(10^{-4})$	0.024
8	0.25	0.5	0.25	294	0.036	0.056	$1.88(10^{-4})$	$2.41(10^{-4})$	$2.77(10^{-4})$	0.054
9	0.25	0.25	0.5	310	0.032	0.058	$1.63(10^{-4})$	$2.51(10^{-4})$	$1.03(10^{-4})$	0.041
10	1/3	1/3	1/3	351	0.032	0.058	$1.63(10^{-4})$	$2.51(10^{-4})$	$1.61(10^{-4})$	0.028

Note: Metrics are defined as in the section on the case study.

some intuition about the magnitude of error introduced, Fig. 7 shows a comparison of the true and reduced set hazard curves for the sites for which 90% of matches are worse.

The errors also should not introduce bias. Fig. 8 shows histograms of the errors, suggesting no notable bias. Maps of the ground motion and liquefaction errors at 475-year return period (Figs. 9 and 10), suggest no geographic bias either. Similar maps for other return periods lead to similar conclusions (Figs. S1–S8).

Finally, Fig. 11 shows the results of the damage analysis. It compares the annual probability distributions of the number of damaged pipes in Los Angeles based on the conventional MCS with 343,891 multihazard scenarios and based on reduced sets of 198 and 351 multihazard scenarios, suggesting relatively small differences compared to the vast reduction in computational demand. The mean damage curve error (MDCE) is 0.028 for the reduced set of 351 multihazard scenarios. Overall, given other uncertainties in a damage or loss analysis, these errors are reasonable for many applications. More or fewer multihazard scenarios could be included in the final set, however, depending on the desired tradeoff between error and computational efficiency. The set of sites i and/or return periods r could be modified to achieve fewer scenarios or smaller errors as well. While computational savings will depend on the particulars of the case study and hardware, in this case computing the pipe damage required approximately 3.5 h for the full set of 343,891 multihazard scenarios when parallelized across 35 nodes on a computing cluster (approximately 120 h without parallelization). It only required nine minutes for the reduced set of 351 multihazard scenarios.

Sensitivity to Objective Function Weights

To examine the effect of considering multiple hazards, we conducted sensitivity analysis on the hazard weights, k_G, k_L, and k_S. Specifically, we did 10 runs in which the weight for each hazard was varied from zero (the hazard was not considered at all) to one (it was the only hazard considered) (Table 1). Not surprisingly, as the weight for a specified hazard (e.g., ground motion) was increased, the errors associated with that hazard decreased. Runs 1, 2, and 3 provide the minimum error possible for ground motion, liquefaction, and surface fault rupture, respectively. Runs 1–6 also suggest that when the weight for a specified hazard goes to zero, the errors can be quite large for that hazard. That is, matching one hazard has an effect on matching the other hazards, but it does not match them very well. When $k_G = 0$ in Runs 2, 3, and 6, for example, the $MHCE_G$ is on the order of 25% to 57% compared to 2.7% when $k_G = 1$. Nevertheless, the results also suggest minimal difference in errors for each hazard when the weight is between 0.25 and 0.5. Overall, Table 1 indicates that as long as the weight for each hazard is at least 0.25, the errors for all hazards are kept small enough for practical purposes.

Conclusions

In this paper, we introduce a new multihazard version of the OPS method of developing a computationally efficient, set of hazard scenarios for use in analysis of spatially distributed infrastructure. It retains the general approach of the previous version (Manzour et al. 2016), but includes liquefaction potential and surface fault rupture in addition to ground motion. The application to Los Angeles indicates that while more scenarios are required for the multihazard analysis to achieve a similar match in a ground motion only analysis, it is still possible to achieve errors small enough for practical purposes with on the order of a few hundred multihazard scenarios. In addition, the sensitivity analysis suggests that developing an ensemble of multihazard scenarios by matching one hazard type does not necessarily indirectly achieve a good match for others. However, as long as the weight for each hazard is at least 0.25, the errors for all hazards are kept small enough for practical purposes.

Opportunities for future research remain. Improved liquefaction and surface fault rupture component models could be incorporated. Additional co-occurring hazards, such as landslide, could be included in a similar way. More applications in more places may strengthen the conclusion that the method can produce excellent results anywhere. Finally, although it was not considered necessary in this case study, it could be useful to develop a new solution algorithm for the Step 5 optimization for cases when there is a larger number of candidate multihazard scenarios and a small number allowed in the final reduced set.

Data Availability Statement

Some or all data, models, or code that support the findings of this study are available from the corresponding author upon reasonable request (code, input data, final set of multihazard scenarios).

Acknowledgments

The authors thank the National Science Foundation (CMMI-1735483) for financial support of this research. The statements, findings, conclusions are those of the authors and do not necessarily reflect the views of the National Science Foundation. This research was also supported in part through Information Technologies

resources at the University of Delaware, specifically high performance computing resources.

Supplemental Materials

Figs. S1–S8 are available online in the ASCE Library (www.ascelibrary.org).

References

Anbazhagan, P., A. Uday, S. Moustafa, and N. Al-Arifi. 2016. "Correlation of densities with shear wave velocities and SPT N values." *J. Geophys. Eng.* 13 (3): 320–341. https://doi.org/10.1088/1742-2132/13/3/320.

Andrus, R., and K. Stokoe. 2000. "Liquefaction resistance of soils from shear-wave velocity." *J. Geotech. Geoenviron. Eng.* 126 (11): 1015–1025. https://doi.org/10.1061/(ASCE)1090-0241(2000)126:11(1015).

Apivatanagul, P., R. Davidson, B. Blanton, and L. Nozick. 2011. "Long-term regional hurricane hazard analysis for wind and storm surge." *Coastal Eng.* 58 (6): 499–509. https://doi.org/10.1016/j.coastaleng.2011.01.015.

Bagriacik, A., R. Davidson, M. Hughes, B. Bradley, and M. Cubrinovski. 2018. "Comparison of statistical and machine learning approaches to modeling earthquake damage to water pipelines." *Soil Dyn. Earthquake Eng.* 112 (Sep): 76–88. https://doi.org/10.1016/j.soildyn.2018.05.010.

Baska, D. 2003. *An analytical/empirical model for prediction of lateral spread displacements*. Seattle: Univ. of Washington.

Boore, D. M. 2004. "Estimating vs(30) (or NEHRP Site Classes) from shallow velocity models (depths 30 m)." *Bull. Seismol. Soc. Am.* 94 (2): 591–597. https://doi.org/10.1785/0120030105.

California Department of Water Resources. 2019. "Water data library—Groundwater level data." Accessed June 1, 2019. http://wdl.water.ca.gov/waterdatalibrary/groundwater/.

Chang, S., M. Shinozuka, and J. Moore. 2000. "Probabilistic earthquake scenarios: Extending risk analysis methodologies to spatially distributed systems." *Earthquake Spectra* 16 (3): 557–572. https://doi.org/10.1193/1.1586127.

Christou, V., P. Bocchini, M. Iranda, and A. Karamlou. 2018. "Effective sampling of spatially correlated intensity maps using hazard quantization: Application to seismic events." *J. Risk Uncertainty Eng. Syst.* 4 (1): 04017035. https://doi.org/10.1061/AJRUA6.0000939.

Clarke, J., and E. Obrien. 2016. "A multi-hazard risk assessment methodology, stress test framework and decision support tool for transport infrastructure networks." *Transp. Res. Procedia* 14 (Jan): 1355–1363. https://doi.org/10.1016/j.trpro.2016.05.208.

Crowley, H., and J. J. Bommer. 2006. "Modelling seismic hazard in earthquake loss models with spatially distributed exposure." *Bull. Earthquake Eng.* 4: 249–273. https://doi.org/10.1007/s10518-006-9009-y.

Cubrinovski, M., et al. 2011. *Liquefaction impacts on pipe networks engineering*. Canterbury, UK: Univ. of Canterbury.

Davis, C. A. 2019. *Performance based seismic design for LADWP water system*. Los Angeles: Los Angeles Department of Water and Power.

De Risi, R., F. De Luca, O. Kwon, and A. Sextos. 2018. "Scenario-based seismic risk assessment for buried transmission gas pipelines at regional scale." *J. Pipeline Syst. Eng. Pract.* 9 (4): 04018018. https://doi.org/10.1061/(ASCE)PS.1949-1204.0000330.

Du, W., and G. Wang. 2014. "Fully probabilistic seismic displacement analysis of spatially distributed slopes using spatially correlated vector intensity measures." *Earthquake Eng. Struct. Dyn.* 43 (5): 661–679. https://doi.org/10.1002/eqe.2365.

FEMA. 2003. *Multi-hazard loss estimation methodology, earthquake model, HAZUS-MH MR4 technical manual*. Washington, DC: FEMA.

Field, E., et al. 2014. "Uniform California earthquake rupture forecast, version 3 (UCERF3)—The time-independent model." *Bull. Seismol. Soc. Am.* 104 (3): 1122–1180. https://doi.org/10.1785/0120130164.

Greiving, S. 2006. *Natural and technological hazards and risks affecting the spatial development of European regions*. Espoo, Finland: Geological Survey of Finland.

Han, Y., and R. Davidson. 2012. "Probabilistic seismic hazard analysis for spatially distributed infrastructure." *Earthquake Eng. Struct. Dyn.* 41 (15): 2141–2158. https://doi.org/10.1002/eqe.2179.

INFRARISK. 2019. "Drupal | Novel Indicators for identifying critical INFRAstructure at RISK from natural hazards." Accessed May 31, 2019. http://www.infrarisk-fp7.eu/.

Iwasaki, T., T. Arakawa, and K. Tokida. 1984. "Simplified procedures for assessing soil liquefaction during earthquakes." *Int. J. Soil Dyn. Earthquake Eng.* 3 (1): 49–58. https://doi.org/10.1016/0261-7277(84)90027-5.

Jayaram, N., and J. Baker. 2010. "Efficient sampling and data reduction techniques for probabilistic seismic lifeline risk assessment." *Earthquake Eng. Struct. Dyn.* 39 (10): 1109–1131. https://doi.org/10.1002/eqe.988.

Juang, C., S. Yang, and H. Yuan. 2005. "Model uncertainty of shear wave velocity-based method for liquefaction potential evaluation." *J. Geotech. Geoenviron. Eng.* 131 (10): 1274–1282. https://doi.org/10.1061/(ASCE)1090-0241(2005)131:10(1274).

Kappes, M., M. Keiler, K. von Elverfeldt, and T. Glade. 2012. "Challenges of analyzing multi-hazard risk: A review." *Nat. Hazards* 64 (2): 1925–1958. https://doi.org/10.1007/s11069-012-0294-2.

Kayen, R., R. Moss, E. Thompson, R. Seed, K. Cetin, A. Der Kiureghian, Y. Tanaka, and K. Tokimatsu. 2013. "Shear-wave velocity-based probabilistic and deterministic assessment of seismic soil liquefaction potential." *J. Geotech. Geoenviron. Eng.* 139 (3): 407–419. https://doi.org/10.1061/(ASCE)GT.1943-5606.0000743.

Kongar, I., T. Rossetto, and S. Giovinazzi. 2017. "Evaluating simplified methods for liquefaction assessment for loss estimation." *Nat. Hazards Earth Syst. Sci.* 17 (5): 781–800. https://doi.org/10.5194/nhess-17-781-2017.

LADWP (Los Angeles Department of Water and Power). 2017. *2016-17 water infrastructure plan distribution mainline*. Los Angeles: LADWP.

Legg, M., L. Nozick, and R. Davidson. 2010. "Optimizing the selection of hazard-consistent probabilistic scenarios for long-term regional hurricane loss estimation." *Struct. Saf.* 32 (1): 90–100. https://doi.org/10.1016/j.strusafe.2009.08.002.

Manzour, H., R. Davidson, N. Horspool, and L. Nozick. 2016. "Seismic hazard and loss analysis for spatially distributed infrastructure in Christchurch, New Zealand." *Earthquake Spectra* 32 (2): 697–712. https://doi.org/10.1193/041415eqs054m.

Maurer, B., R. Green, M. Cubrinovski, and B. Bradley. 2014. "Evaluation of the liquefaction potential index for assessing liquefaction hazard in Christchurch, New Zealand." *J. Geotech. Geoenviron. Eng.* 140 (7): 04014032. https://doi.org/10.1061/(ASCE)GT.1943-5606.0001117.

Mayfield, R., S. Kramer, and Y. Huang. 2010. "Simplified approximation procedure for performance-based evaluation of liquefaction potential." *J. Geotech. Geoenviron. Eng.* 136 (1): 140–150. https://doi.org/10.1061/(ASCE)GT.1943-5606.0000191.

Miller, M., and J. Baker. 2015. "Ground-motion intensity and damage map selection for probabilistic infrastructure network risk assessment using optimization." *Earthquake Eng. Struct. Dyn.* 44 (7): 1139–1156. https://doi.org/10.1002/eqe.2506.

Omidvar, B., and H. Kivi. 2016. "Multi-Hazard failure probability analysis of gas pipelines for earthquake shaking, ground failure and fire following earthquake." *Nat. Hazards* 82 (1): 703–720. https://doi.org/10.1007/s11069-016-2214-3.

O'Rourke, T., S. Jeon, S. Toprak, M. Cubrinovski, M. Hughes, S. van Ballegooy, and D. Bouziou. 2014. "Earthquake response of underground pipeline networks in Christchurch, NZ." *Earthquake Spectra* 30 (1): 183–204. https://doi.org/10.1193/030413EQS062M.

Petersen, M., T. Dawson, R. Chen, T. Cao, C. Wills, D. Schwartz, and A. Frankel. 2011. "Fault displacement hazard for strike-slip faults." *Bull. Seismol. Soc. Am.* 101 (2): 805–825. https://doi.org/10.1785/0120100035.

Powers, P. 2015. "GitHub—usgs/nshm-cous-2014: NSHM: Conterminous U.S. 2014." Accessed June 1, 2018. https://github.com/usgs/nshm-cous-2014.

Salman, A. M., and Y. Li. 2018. "A probabilistic framework for multi-hazard risk mitigation for electric power transmission systems subjected to seismic and hurricane hazards." *Struct. Infrastruct. Eng.* 14 (11): 1499–1519. https://doi.org/10.1080/15732479.2018.1459741.

SCG (Southern California Gas Company). 2003. *Liquefaction susceptibility maps*. Los Angeles: SCG.
Seed, H., and I. Idriss. 1971. "Simplified procedure for evaluating soil liquefaction potential." *ASCE J. Soil Mech. Found. Div.* 97 (9): 1249–1273.
Soleimani, N. 2020. "Develop a probabilistic scenario-based model of the risk of multiple infrastructure systems to earthquakes." Ph.D. dissertation, Dept. of Civil and Environmental Engineering, Univ. of Delaware.
US Census Bureau. 2019. "Population." Accessed November 2, 2019. https://www.Census.gov.
Vaziri, P., R. Davidson, P. Apivatanagul, and L. Nozick. 2012. "Identification of optimization-based probabilistic earthquake scenarios for regional loss estimation." *J. Earthquake Eng.* 16 (2): 296–315. https://doi.org/10.1080/13632469.2011.597486.
Wills, C., and K. Clahan. 2006. "Developing a map of geologically defined site-condition categories for California." *Bull. Seismol. Soc. Am.* 96 (4): 1483–1501. https://doi.org/10.1785/0120050179.
Youd, T., C. Hansen, and S. Bartlett. 2002. "Revised multilinear regression equations for prediction of lateral spread displacement." *J. Geotech. Geoenviron. Eng.* 128 (12): 1007–1017. https://doi.org/10.1061/(ASCE)1090-0241(2002)128:12(1007).
Zhu, J., L. Baise, and E. Thompson. 2017. "An updated geospatial liquefaction model for global application." *Bull. Seismol. Soc. Am.* 107 (3): 1365–1385. https://doi.org/10.1785/0120160198.
Zolfaghari, M., and E. Peyghaleh. 2016. "Development of optimization-based probabilistic earthquake scenarios for the city of Tehran." *Comput. Geosci.* 86 (Jan): 129–145. https://doi.org/10.1016/j.cageo.2015.10.003.